
This is an electronic reprint of the original article.
This reprint may differ from the original in pagination and typographic detail.

Laurila, Tomi; Sainio, Sami; Jiang, Hua; Isoaho, Noora; Koehne, Jessica; Etula, Jarkko; Koskinen, Jari; Meyyappan, M.

Application-Specific Catalyst Layers

Published in:
ACS Omega

DOI:
[10.1021/acsomega.6b00441](https://doi.org/10.1021/acsomega.6b00441)

Published: 13/02/2017

Document Version
Publisher's PDF, also known as Version of record

Published under the following license:
CC BY-NC

Please cite the original version:
Laurila, T., Sainio, S., Jiang, H., Isoaho, N., Koehne, J., Etula, J., Koskinen, J., & Meyyappan, M. (2017). Application-Specific Catalyst Layers: Pt-Containing Carbon Nanofibers for Hydrogen Peroxide Detection. *ACS Omega*, 2(2), 496-507. <https://doi.org/10.1021/acsomega.6b00441>

This material is protected by copyright and other intellectual property rights, and duplication or sale of all or part of any of the repository collections is not permitted, except that material may be duplicated by you for your research use or educational purposes in electronic or print form. You must obtain permission for any other use. Electronic or print copies may not be offered, whether for sale or otherwise to anyone who is not an authorised user.

Application-Specific Catalyst Layers: Pt-Containing Carbon Nanofibers for Hydrogen Peroxide Detection

Tomi Laurila,^{*,†} Sami Sainio,[†] Hua Jiang,[‡] Noora Isoaho,[†] Jessica E. Koehne,[§] Jarkko Etula,^{||} Jari Koskinen,^{||} and M. Meeyappan[§]

[†]Department of Electrical Engineering and Automation, School of Electrical Engineering, Aalto University, Tietotie 3, Espoo 02150, Finland

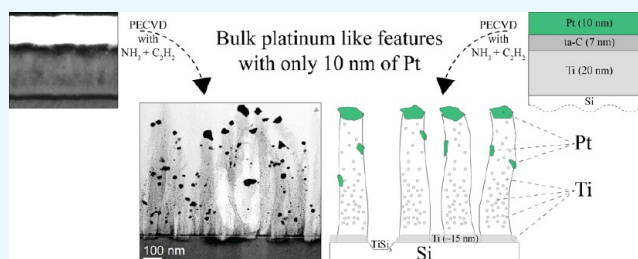
[‡]Department of Applied Physics, School of Science, Aalto University, Puumiehenkuja 2, Espoo 02150, Finland

[§]Center for Nanotechnology, NASA Ames Research Center, Moffett Field, Mountain View, California 94035, United States

^{||}Department of Chemistry and Materials Science, School of Chemical Technology, Aalto University, Kemistintie 1, Espoo 02150, Finland

Supporting Information

ABSTRACT: Complete removal of metal catalyst particles from carbon nanofibers (CNFs) and other carbon nanostructures is extremely difficult, and the envisioned applications may be compromised by the left-over impurities. To circumvent these problems, one should use, wherever possible, such catalyst materials that are meant to remain in the structure and have some application-specific role, making any removal steps unnecessary. Thus, as a proof-of-concept, we present here a nanocarbon-based material platform for electrochemical hydrogen peroxide measurement utilizing a Pt catalyst layer to grow CNFs with intact Pt particles at the tips of the CNFs. Backed by careful scanning transmission electron microscopy analysis, we show that this material can be readily realized with the Pt catalyst layer thickness impacting the resulting structure and also present a growth model to explain the evolution of the different types of structures. In addition, we show by electrochemical analysis that the material exhibits characteristic features of Pt in cyclic voltammetry and it can detect very small amounts of hydrogen peroxide with very fast response times. Thus, the present sensor platform provides an interesting electrode material with potential for biomolecule detection and in fuel cells and batteries. In the wider range, we propose a new approach where the selection of catalytic particles used for carbon nanostructure growth is made so that (i) they do not need to be removed and (ii) they will have essential role in the final application.



INTRODUCTION

Despite its simple structure, hydrogen peroxide (H_2O_2) has a widespread usage ranging all the way from industrial to alimentary and clinical applications. It can be either electrochemically oxidized to O_2 ($E^0 = 0.695 \text{ V}$) or reduced to water ($E^0 = 1.763 \text{ V}$) in diffusion-controlled two-electron processes.¹ Hydrogen peroxide and its redox reactions are closely linked to fuel cell technology as it is formed as a reaction intermediate in the oxygen reduction reaction.^{1–3} Furthermore, H_2O_2 is formed as a byproduct in various enzymatic reactions such as those catalyzed by glucose oxidase,⁴ glutamate oxidase,⁵ and cholesterol oxidase.⁶ Enzymatic production makes H_2O_2 feasible for biosensor applications as it can be indirectly detected at lower potentials compared to the enzyme substrate molecules. However, H_2O_2 is typically detected indirectly in sensor applications by its chemical interaction with metallic electrode surfaces, which then produce the current, as is the case, for example, with Pt.

Pt-based electrodes have been frequently used to detect hydrogen peroxide.^{8–10} Likewise, carbon-based nanostructures

in the form of nanotubes and nanofibers have been extensively used in the detection of different biomolecules via and without enzymatic detection.^{11–17} The structure of oriented carbon nanofibers (CNFs) is especially ideal for enzyme linking without any additional polymer layers. For example, glutamate detection via enzymatic reaction that produces hydrogen peroxide with various metal-particle-containing carbon nanotubes (CNTs) and CNFs has been demonstrated.^{18,19} These metal particles typically remain in the catalyst layers used to grow the carbon nanostructures that stay on the tubes or fibers despite the cleaning procedures. Consequently, unwanted electrochemical features are often introduced and the interpretation and control of the reactions taking place in the systems become complicated. On the basis of the available information, it appears that carbon alone is not as active toward the hydrogen peroxide as the carbon hybrids containing

Received: November 29, 2016

Accepted: January 25, 2017

Published: February 13, 2017

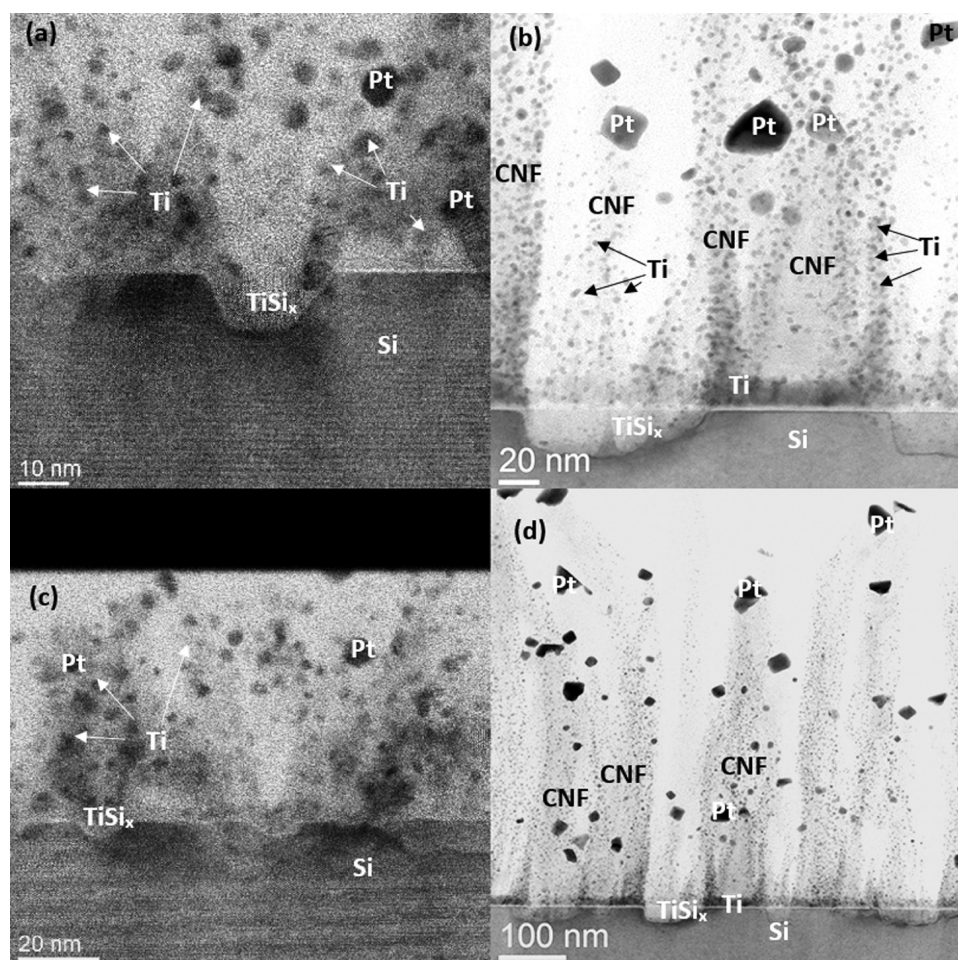


Figure 1. Scanning transmission electron microscopy (STEM) micrographs of CNFs grown on (a) 2 nm thick Pt and (b) 10 nm thick catalyst layer, with higher-magnification images in (c) and (d).

metallic nanoparticles. Hence, we introduce the concept of utilizing application-specific catalyst layers in this article to realize carbon nanostructures where metallic nanoparticles on the tips of the nanostructures are present not because they are optimum for the growth process but because they have a specific electrochemical role in the final structure. This approach requires no removal procedures as the remaining metallic catalyst is actually needed for the intended application. Thus, as a proof-of-concept, we combine here the structural features of CNFs with the known electrocatalytic properties of Pt to demonstrate the growth of Pt-containing CNFs and show that they can be used for hydrogen peroxide detection with high sensitivity. The objective is to fabricate a structure with a high amount of small catalytic particles that do not experience coarsening during continuous use and that are directly electrically connected to the electrode surface. Detailed high-resolution transmission electron microscopy (HRTEM) analysis combined with the electrochemical characterization is utilized to support our arguments and rationalize the growth of these novel materials.

RESULTS

Structure. Figure 1 shows the resulting structures from the growth process for two different Pt layer thicknesses. The 2 nm thick Pt catalyst layer did not produce proper fibers; instead, formation of cone-like structures with a large number of small Ti particles randomly scattered throughout the structure is seen.

The height of these cone-like features is on the order of a few tens of nanometers. One can also clearly observe that the Ti layer has reacted with Si to form Ti-silicide (most likely TiSi_2); consequently, there are many characteristic trenches for the silicide formation reaction at the Si interface. In addition, there is no continuous Ti layer on top of Si, but the Ti is either distributed inside the cone-like structures or incorporated in the Ti-silicide, as shown by energy-dispersive spectrometer (EDS) elemental map (Supporting Information). Pt is also similarly distributed within the whole reaction zone.

In contrast, the 10 nm thick Pt catalyst layer has produced CNFs. The length of the fibers is typically a few hundreds of nanometers, but some structures are up to the micrometer scale. Again, one can see a fairly large number of finely dispersed Ti particles along the body of the fiber. However, Pt particles are also seen at the tip of the fibers (Figure 2), which was not the case with the cone-like structures. In addition, the original Ti layer is still mostly preserved at the Si/Ti interface in contrast to the samples with the 2 nm thick Pt layer (see EDS elemental maps in Supporting information) despite the formation of Ti-silicide(s) at some locations. A notable feature is that the CNFs appear to adhere to the surface only from the locations where the Ti layer is still intact and not where Ti-silicide formation has taken place. Thus, this underlines the role of Ti as the adhesion layer in our structure. Despite the fact that the 10 nm thick Pt catalyst layer does produce CNFs, the

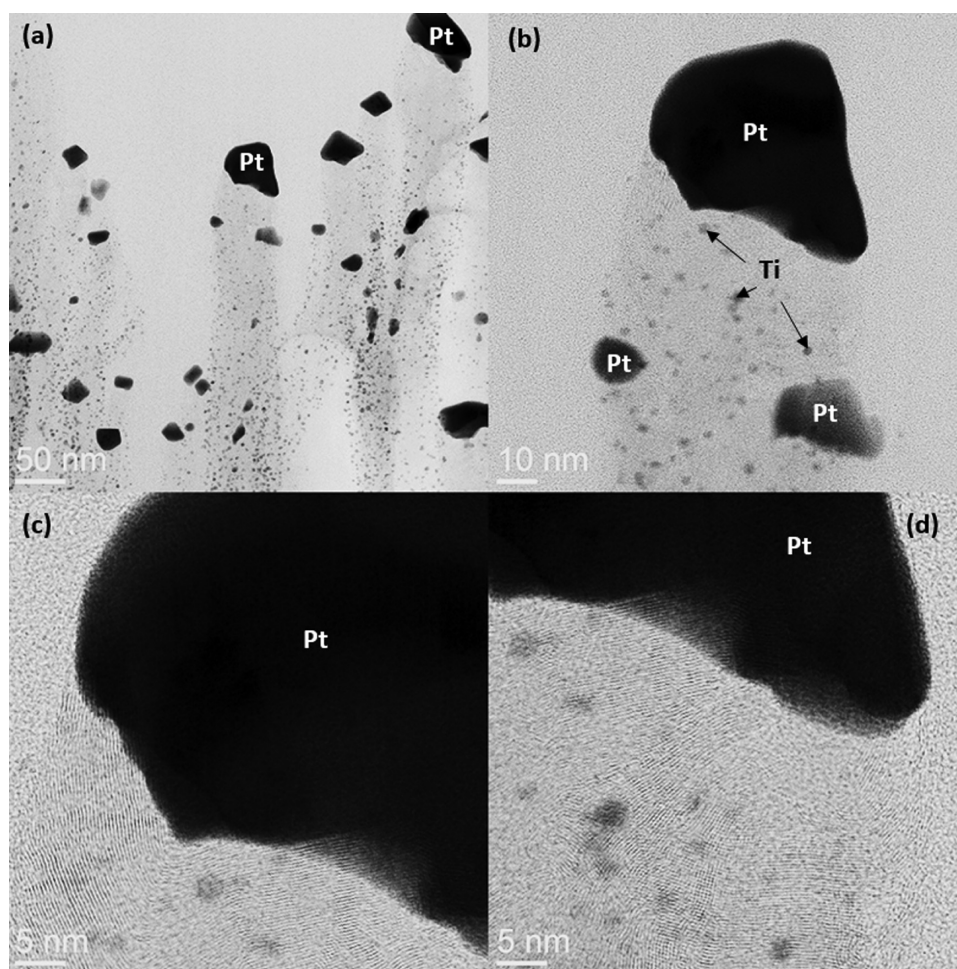


Figure 2. STEM micrographs of CNFs grown with the 10 nm thick Pt catalyst layer with higher magnifications: (a) overview of the structure, (b) higher-magnification micrograph showing some Ti particles near the larger Pt particles, and (c, d) high-magnification micrographs showing the interfacial structure between the Pt particle and the graphene planes of the CNFs.

growth kinetics is rather slow when compared to that of the same process with Ni catalyst.^{20,21}

Higher-magnification imaging of the CNFs grown with the 10 nm Pt catalyst layer reveals several features: (i) in most cases, the Pt can be found exclusively at the tip of the CNF as a particle. At some locations, it appears that Pt particles are also distributed along the fiber body, but this represents a minority case. In addition, in many cases, this may be a result of fibers of different lengths crossing each other. (ii) Pt particles at the tip of the fibers do not seem to have any specific shape or size, but they are more or less of random orientation and size. This is likely to be a result of the mostly repulsive interaction between Pt and C as discussed later on. However, the structure seems to be single crystal. (iii) The number of finely dispersed Ti particles strongly decreases as one moves from the root of the fiber toward the tip. (iv) The ordering of graphene planes in the fibers and around the Pt particles is not so pronounced as with other catalyst materials such as Ni,^{20,21} which again most likely has its origin on the repulsive interaction between Pt and C.

Electrochemistry. Only the CNF/Pt samples with the 10 nm Pt catalyst layer produced clear Pt-type characteristics during cyclic voltammetry. This indicates that the amount of exposed Pt was not high enough with the samples grown from the 2 nm Pt catalyst layer. Therefore, only the results from the

samples with the 10 nm Pt layer are presented here in Figure 3a, showing the cyclic voltammogram of the CNF/Pt hybrid material in 0.15 M H₂SO₄. A similar voltammogram for the polycrystalline thin-film Pt sample is shown in Figure 3b, and Pt-like features are evident from a comparison of Figure 3a,b. At the anodic end of Figure 3a, one can see the shoulder related to the formation of Pt-oxide although it is not possible to observe clearly all the three peaks corresponding to the gradual formation process of Pt-oxide on polycrystalline Pt in ultrahigh-purity H₂SO₄.²² Also, the reduction peak of Pt-oxide is clear with the CNF/Pt electrode. Likewise, at the cathodic end, the hydrogen adsorption and desorption peaks are evident although they are not as clearly exhibited as with the thin-film Pt sample. The slight attenuation of the Pt features in the case of CNF/Pt samples might be caused by impurities present in the system. However, as the current at the anodic end does not rise significantly at the Pt-oxide formation region, the amount of oxidizable impurities is not expected to be very high. In fact, the most likely origin of any oxidizable and other impurities in the case of CNF/Pt electrodes would be the samples themselves. Therefore, we believe that we can to a large extent ignore these minor additional features in the electrochemistry of these samples. Thus, we can state that the CNF/Pt electrode clearly shows the features of polycrystalline Pt, indicating that the Pt particles present in the structure are not predominantly of

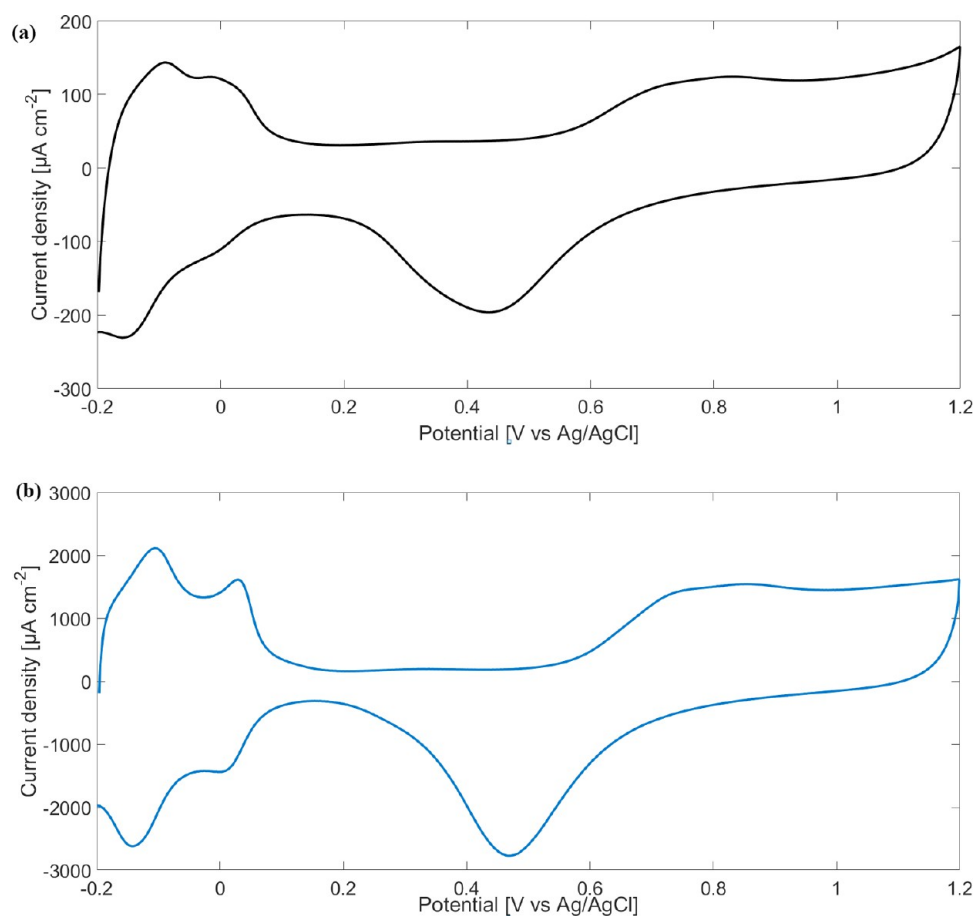


Figure 3. Cyclic voltammograms in 0.15 M H_2SO_4 of (a) CNF/Pt(10 nm) and (b) thin film of Pt (4 nm) on the Si/Ti sample. The cycling speed is 50 mV/s.

certain orientation (e.g., only (111) or (200)) but more or less randomly oriented. The notable differences between the CNF/Pt and thin-film polycrystalline Pt samples include (i) the cathodic shift and less-well-defined shape of the Pt-oxide reduction peak and (ii) the narrower double-layer region and higher background current density in the case of the CNF/Pt electrode. These differences are likely to be a result of CNF/Pt having a higher active area than that of the geometrically same-sized thin-film Pt electrode and because Pt is in the form of nanoparticles instead of a film, as discussed later on. It is to be noted that there is no observable electrochemical effect from the Ti nanoparticles embedded within the CNF.

Figure 4a shows the results from the chronoamperometry measurements with different amounts of H_2O_2 in phosphate-buffered saline (PBS) with the CNF/Pt (10 nm) samples. The potential is stepped to -0.1 V versus Ag/AgCl reference, that is, to the double-layer region, and the solutions were not purged with argon. The reasons for these choices are that (i) we are detecting the reduction current originating from the reduction of the unstable Pt-oxide formed as a consequence of the chemical decomposition of H_2O_2 on the originally metallic Pt and that (ii) we need to assess if oxygen, which is inevitably present under the *in vivo* conditions, would disturb our measurements. Details of the mechanism related to (i) are described elsewhere.^{7,9} As can be seen in Figure 4, the presence of hydrogen peroxide increases the cathodic current that starts to significantly deviate from the charging current already after 20 ms although the differences in the concentrations become

more evident after about 60 ms. Thus, the response time is very fast as required by many applications such as enzymatic glutamate detection for example.²³ Figure 4b shows that the CNF/Pt (10 nm) electrode also has a fairly long linear range for H_2O_2 , which together with the fast response time and high sensitivity makes this material a promising platform for hydrogen peroxide detection.

DISCUSSION

To gain more insight into the growth mechanism responsible for the observed structures, cross-sectional STEM investigations of the as-fabricated and preannealed Si/Ti/ta-C/Pt (2 or 10 nm) samples were carried out.

Figure 5 shows the two types of samples (2 or 10 nm Pt) after the deposition process. The 2 nm Pt catalyst layer shows an uneven rough structure and some discontinuities in the film (Figure 5a,b) whereas the 10 nm Pt layer appears to be uniform with a relatively flat surface (Figure 5c,d). The Ti adhesion layer and ta-C layer are of similar thicknesses and morphologies in both types of samples. The ta-C layer is slightly thinner in both cases than expected (e.g. 5 vs 7 nm). The interface between the Ti and ta-C layers is not particularly sharp in either sample type, indicating some degree of mixing, but there is no evidence of excessive interfacial reaction or interdiffusion after the deposition. There is an additional layer at the Si/Ti interface in both samples, which has been shown to be an oxygen-rich SiO_x type of layer.^{24,25} The above arguments are further confirmed by the dark-field images (Figure 5b,d).

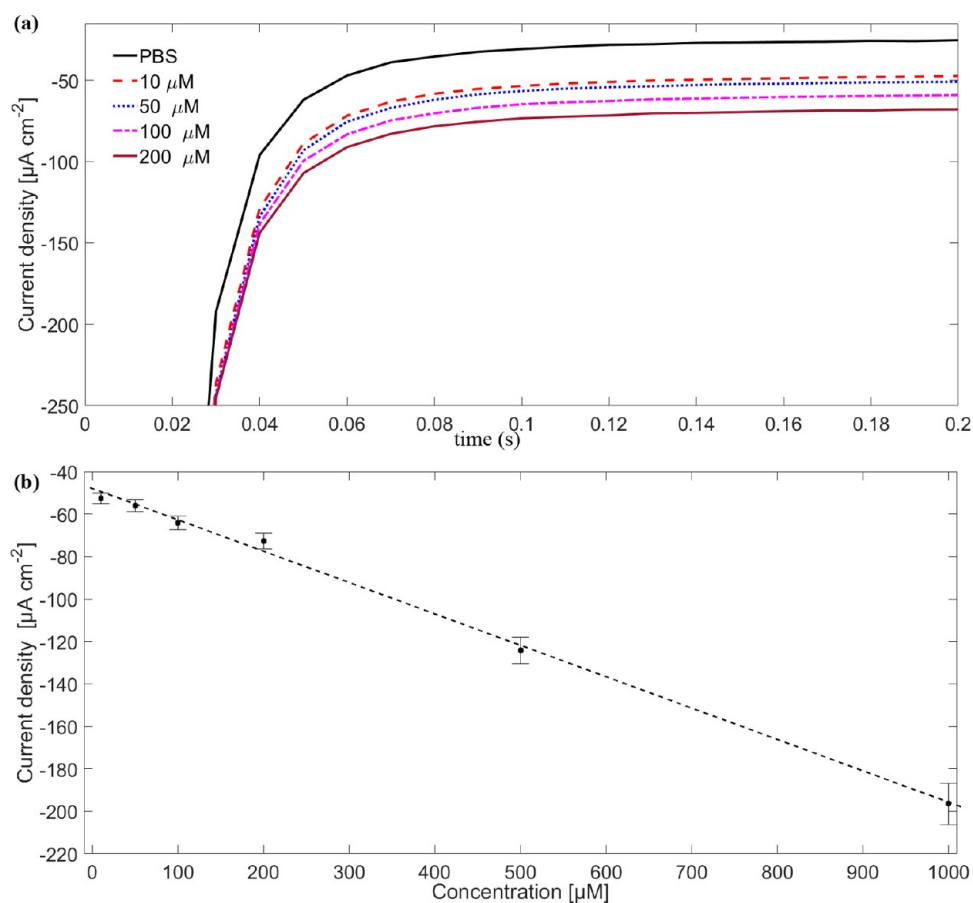


Figure 4. (a) Chronoamperometry measurements (step potential at -0.1 V vs Ag/AgCl) with different concentrations of H_2O_2 with the Si/Ti/ta-C/Pt (10 nm) electrode and (b) dependence of current density on the H_2O_2 concentration.

To obtain further information about the structures of catalyst layers after fabrication, we carried out X-ray reflection (XRR) and grazing incidence angle X-ray diffraction (GIXRD) measurements for the two types of samples. While comparing the GIXRD spectra (Figure 6) for the 2 and 10 nm Pt films, it is evident that there are significant differences in the film structure already after fabrication. Whereas in the 10 nm Pt film all five Pt peaks are clearly present, in the 2 nm Pt film hardly any Pt features can be seen and peaks most likely originating from the underlying Ti and Si layers can also be observed (the peak around 50° , which has not been indexed in Figure 6 as the origin of it is not unambiguously known). This indicates that the 10 nm Pt film is clearly continuous and polycrystalline with no preferred orientation, whereas the 2 nm Pt film is likely to be relatively non-uniform with varying thickness, which is consistent with the STEM micrographs seen in Figure 5a–d. On the basis of the analysis of full width at half-maximum of the Pt peaks, the grain size could be estimated to be in the range of 5 nm in the 10 nm Pt catalyst film. The XRR measurements (Figure S3a,b) from the two types of samples further suggest that whereas the 10 nm Pt film appears to be fully continuous and uniform the 2 nm Pt film appears to be relatively discontinuous, and some mixing with the underlying ta-C film seems to have occurred already during deposition. Thus, on the basis of GIXRD and XRR measurements, the following conclusions can be drawn: (i) the 10 nm Pt catalyst film after deposition is continuous, uniform, and shows no preferential orientation with a grain size on the order of 5 nm, whereas (ii) the 2 nm Pt film appears to be highly non-

uniform and discontinuous. These observations are fully consistent with the STEM results discussed above.

Figure 7 shows the same type of samples as in Figure 5 but now after preannealing, just before the growth stage. The 2 nm Pt layer appears highly irregular and shows a lot of discontinuities as a result of preannealing. In addition, there are some signs of interdiffusion at the ta-C/Pt interface. In contrast, the 10 nm Pt sample shows again a uniform Pt layer on top of ta-C and there is hardly any change in this case when compared to the same type of sample after deposition. Thus, it can be concluded that the 10 nm Pt layer is still uniform and protects the underlying structure after the preannealing stage (just before the growth phase starts), whereas this is clearly not the case with the 2 nm thick Pt layer. This is suggested to lead to the observed differences in the resulting structures as discussed next.

Figure 8 shows the bright-field (a,c) and dark-field (b,d) images of the resulting nanostructures as well as (e) a schematic presentation of the resulting structures, on which we base the following discussion about the details of the growth phenomena. On the basis of the information from the literature and from the results of this work, it is evident that Pt is not a particularly good catalyst for CNF or CNT growth.^{29,30} This is caused most likely by the repulsive interaction between Pt and C, which leads among other things to a very low solubility of graphite to fcc-Pt. In addition, there are no known Pt-carbides (stable or metastable), further highlighting the lack of any attractive interaction between Pt and C. The repulsive interaction between Pt and C by no means excludes the

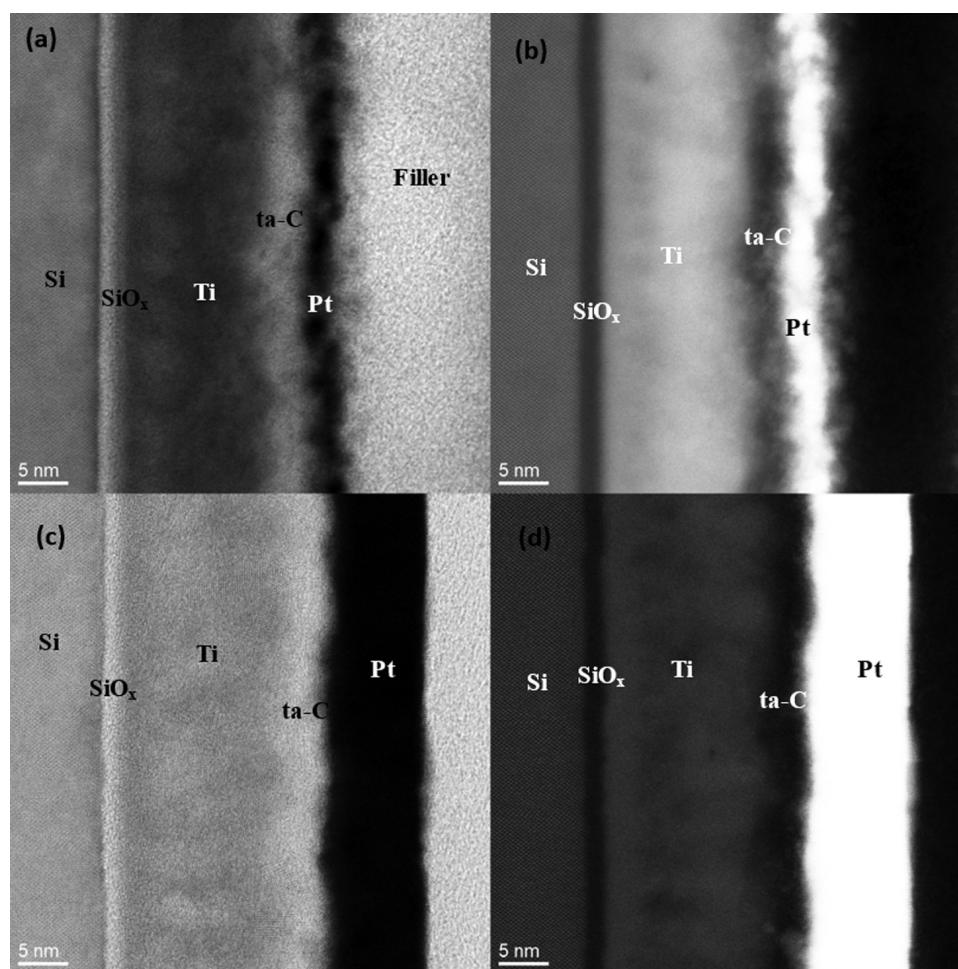


Figure 5. Bright-field and dark-field STEM micrographs from the (a, b) Si/Ti/ta-C/Pt(2 nm) and (c, d) Si/Ti/ta-C/Pt(10 nm) samples after fabrication.

mixing of the elements as the latter process is fundamentally driven by the increase in the configurational entropy of the system. Contributions from the entropy can be expected to overrun any enthalpy contributions (interaction term) quite easily at these relatively high temperatures. However, the lack of favorable interaction between Pt and C leads to a long incubation time at the start of the growth phase. This is the case of the 2 nm thick Pt layer, leading to the disintegration of the whole initial structure owing to the following reasons: (i) on the basis of the micrographs in Figures 5 and 7, as well as GIXRD and XRR results (Figures 6 and S3), the 2 nm Pt layer is highly discontinuous already after the deposition stage and becomes more and more irregular during the preannealing stage before the growth phase starts. (ii) Consequently, the ta-C layer is directly exposed (at least partly) to the acetylene (carbon plasma) in the chamber. When the acetylene decomposes on the surface, it produces mostly carbon and hydrogen.³¹ The hydrogen from the decomposition will etch and graphitize the ta-C thin films (see the Raman results in Figure S4), which then leads to the partial (or total) disappearance of the ta-C film. (iii) As a result, there is no fully protective ta-C film on top of the Ti layer and it will start to react with the incoming carbon, leading to the production of the mixed carbon and titanium cones. Pt is also distributed randomly along the cones as there is practically no “growth” phase in this case (Figure 8a,b).

Some of the Ti also reacts with the underlying Si substrate to produce Ti-silicide, which together with the cone formation results into the disappearance of the original Ti layer. In contrast, the 10 nm Pt film, owing to its uniform morphology after the preannealing stage, manages to protect the underlying ta-C (and consequently also Ti) films until the actual CNF growth phase kicks in. Thus, this results into the observed structure where Pt particles are at the tips of the resulting CNF and most of the Ti layer is still present at the Si interface (Figure 7b,d). Also, the structure of the fibers in this case is somewhat less ordered than, for example, that with Ni catalysts, owing to the repulsive nature of the Pt interaction with the graphene sheets. The Pt particles observed at the CNF tips are mostly single crystals (Figure 9), but their size is too large in general that they could be directly traced back to the original Pt film with the grain size on the order of 5 nm. It is possible that during the initial CNF growth stage the Pt film partly disintegrates and recrystallizes to produce these larger grains that can be found at the tips of the CNF. However, this issue requires further studies. The ta-C layer is again decomposed after the exposure to the growth environment by hydrogen formed during the decomposition of acetylene and perhaps partly used for the CNF growth.

Hence, we can conclude that owing to the repulsive interaction between Pt and C and the resulting relatively poor catalytic properties of Pt for CNF growth, the incubation

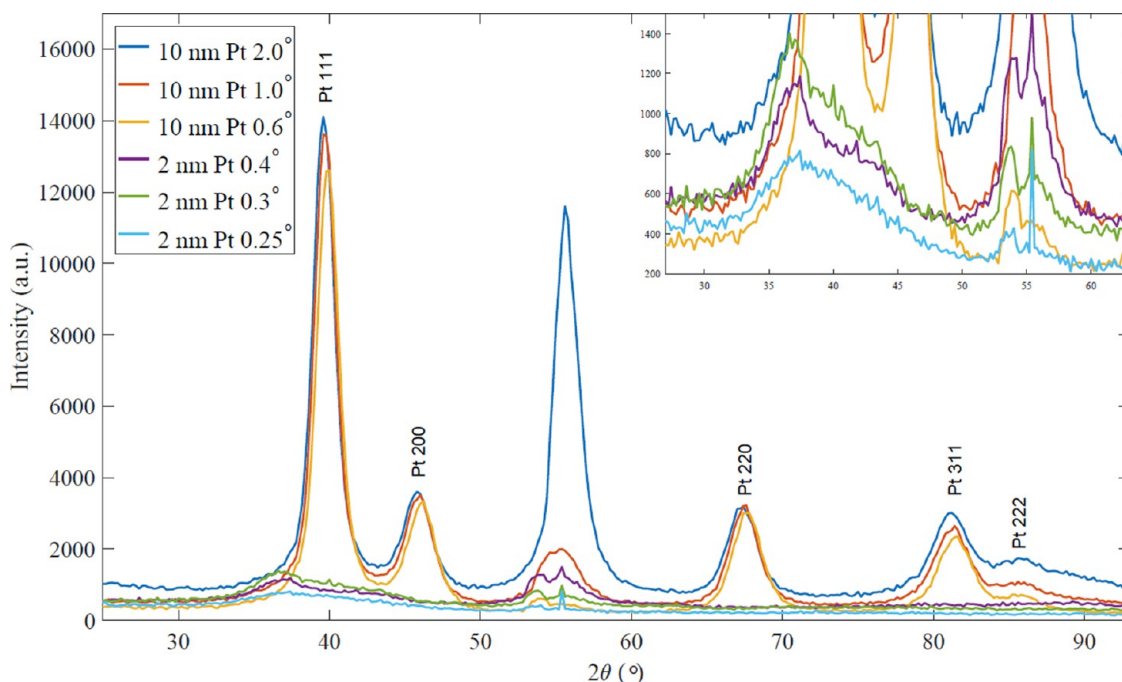


Figure 6. GIXRD spectra from the Si/Ti/ta-C/Pt (10 nm) and Si/Ti/ta-C/Pt (2 nm) samples. The inset shows the magnified view from the region between 30 and 60° (2θ). Note that the peak around 50° could be indexed both to Ti and Si and has therefore been left unindexed. Peaks' locations are based on the data from refs 26–28.

time at the start of the growth becomes long. This then leads to complete disintegration of the Si/Ti/ta-C/Pt (2 nm) structure before any actual growth can occur, subsequently leading to the observed cone-type structures where Ti and Pt particles are randomly scattered along the disordered structure. In contrast, the 10 nm Pt catalyst layer is able to protect the underlying structure from disintegration until the actual growth phase starts and therefore leads to the observed CNF structures where Pt particles sit on the top of the fibers and are not randomly scattered in the reaction zone.

The electrochemical features seen in Figure 3 and especially the cathodic shift in the Pt-oxide reduction potential and the shape of the peak can be understood on the basis of the above discussion. The reduction peak is shifted cathodically with respect to that of the thin-film Pt electrode, owing to the small size of the Pt particles at the tip of the CNF, which leads to a higher adsorption strength of OH on these particles in comparison to that on the Pt thin film, as shown in refs 32, 33. Thus, the reduction of the Pt-oxide becomes harder than that in the case of a uniform (“infinite”) Pt film. The electrode shown in Figure 3a has been cycled already ca. 50 cycles before recording the voltammogram in the figure. This exemplifies the stability of the CNF-anchored nanoparticles as the Pt-oxide reduction peak does not become narrower and shifts back to that of bulk Pt, which would indicate significant coarsening/agglomeration of the structure³⁴ even with this prolonged cycling. Thus, the desired high active catalyst area is retained. This is a clear advantage over conventional Pt nanoparticle carbon hybrids where Pt is deposited on top of an existing carbon structure and can be expected to be beneficial not only in basic research of nanoparticle electrochemistry but also, for example, in fuel cell technology. In addition, as shown in Figure 8, there is a relatively large size distribution among the Pt particles. This is suggested to lead to the broadening of the Pt-oxide reduction peak as the OH adsorption strength will change

as a function of the Pt particle size³³ and lead to a gradual reduction (thus wide peak) reaction where largest particles are reduced first followed by the smaller ones. Finally, the various single Pt crystals at the CNF tips must possess different orientations as the voltammogram clearly shows features of polycrystalline Pt without any signs of electrochemical response arising from only certain orientations of Pt films, such as (111), (110), and (100).³⁵

The amperometric response of our structure toward H_2O_2 is shown in Figure 4. The current density (circular sample area, $r = 1.5$ mm) was averaged between 0.05 and 0.2 s from step 2 to evaluate the linear response. Between 10 and 1000 μM , the ta-C/CNF hybrid shows a linear behavior with a limit of detection of ~ 0.2 nM (S/N = 3) and sensitivity of $0.1478 \mu\text{A} \mu\text{M}^{-1} \text{cm}^{-2}$ (Table 1). An earlier study with vertically aligned CNFs showed a detection limit of 66 μM and sensitivity of $0.0906 \mu\text{A} \mu\text{M}^{-1} \text{cm}^{-2}$ at anodic current (at 0.6 V vs Ag/AgCl⁴⁸). Here, we have gained significant improvement in sensitivity, over 300 000-fold, at the cathodic end (-0.1 V) when the calculated limit of detection is considered. Thus, incorporating Pt (and only Pt) intentionally to CNF tips has had a significant positive effect on the electrochemical performance of the CNF structure as desired.

Compared to that of other carbon nanomaterials, the improvement in sensitivity is also significant as can be seen from Table 1 and remains unmatched even by Pt nanoparticles on CNTs.³⁶ Also, if one compares the present material to mesoporous Pt⁵⁰ and Pt nanowires,⁵¹ CNF + Pt electrodes outperform these structures significantly both in sensitivity and temporal resolution. The fact that we utilize a reductive potential of -0.1 V (vs Ag/AgCl) most likely reduces the interference from, for example, dopamine and ascorbic acid as these typically oxidize at higher (positive) potentials on carbon-based structures and Pt.^{52–54} Moreover, the response time of our electrode material for H_2O_2 is clearly faster than for any

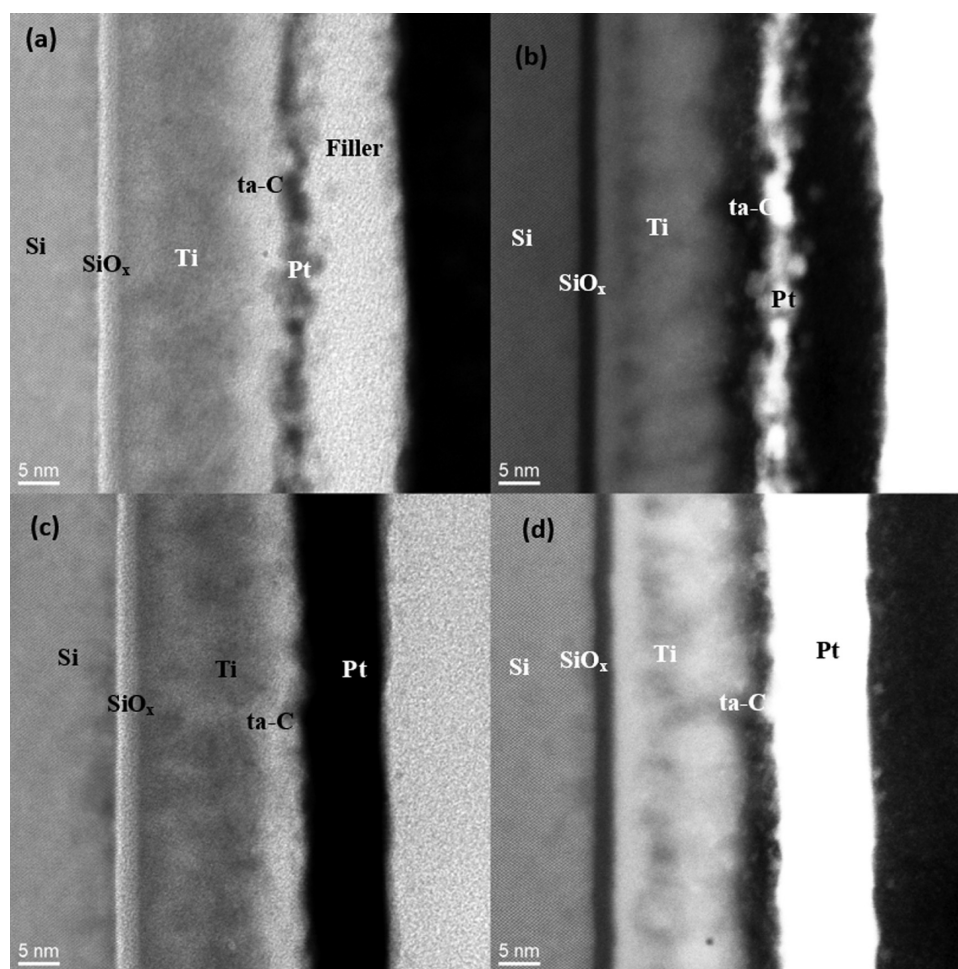


Figure 7. Bright-field and dark-field STEM micrographs from (a, b) Si/Ti/ta-C/Pt(2 nm) and (c, d) Si/Ti/ta-C/Pt(10 nm) samples after preannealing.

other structure shown in Table 1. This is a huge advantage in enzymatic sensing of different biomolecules such as an important neurotransmitter glutamate. In situ detection of glutamate is an extremely difficult task especially owing to the strict temporal and spatial requirements (response times must be few tens of microseconds and measurement probe size approximately 1–5 μm).²³ On the basis of the values shown in Table 1, our structure is the only one that can meet the temporal requirement and has the potential to provide physically meaningful information from in situ measurements. The CNF structure also provides means to meet the spatial requirement as the individual CNF-Pt fibers have diameters less than 100 nm, thus making the present material platform extremely interesting from sensing point of view. This is an important advantage over various other Pt-incorporated carbon nanostructures obtained with electrospinning and subsequent carbonization,^{55–57} as it would be very difficult to realize devices with micrometer or nanometer size dimensions from these ones. Finally, the crucial role of Pt particles at the CNF tips for reaching the present sensitivity and time resolution levels toward H_2O_2 can be appreciated when considering the results from the identical amperometric measurements made by utilizing Pt-free CNFs reported by us earlier in ref 19. In this study, we processed similar CNF structures by the same growth parameters as here but by utilizing nanodiamonds as a catalyst layer, thus achieving metal-free CNF structures. The response

of these structures towards H_2O_2 was significantly weaker than that of the present structure,¹⁹ highlighting the necessity of having the Pt particles at the CNF tips to achieve superior performance. Likewise, in the same study,¹⁹ we also used Ni catalyst (and again the same processing parameters) to grow CNF structures with Ni particles at their tips,¹⁹ but again the performance was of markedly lower quality than that achieved with the CNF/Pt structures in the present study.

CONCLUSIONS

We have introduced a novel concept of using application-specific catalyst material for CNF growth that is meant to stay in the structure. Thus, no metal particle removal steps are required. As a proof-of-concept, we have realized a hybrid structure in which Pt nanoparticles are integrated into CNFs. A growth model to explain the evolution of the different types of structures has been presented with the aid of a detailed TEM analysis. The electrochemical analysis shows that the material reveals characteristic features of Pt and that it can detect small amounts of hydrogen peroxide with very fast response times. The latter is very important in many applications, for example, in enzymatic detection of various biomolecules such as glutamate. Benchmarking the present results to those obtained by CNF or Pt alone highlights that the present hybrid material has performance significantly higher than that of its individual components. Thus, the present material platform provides an

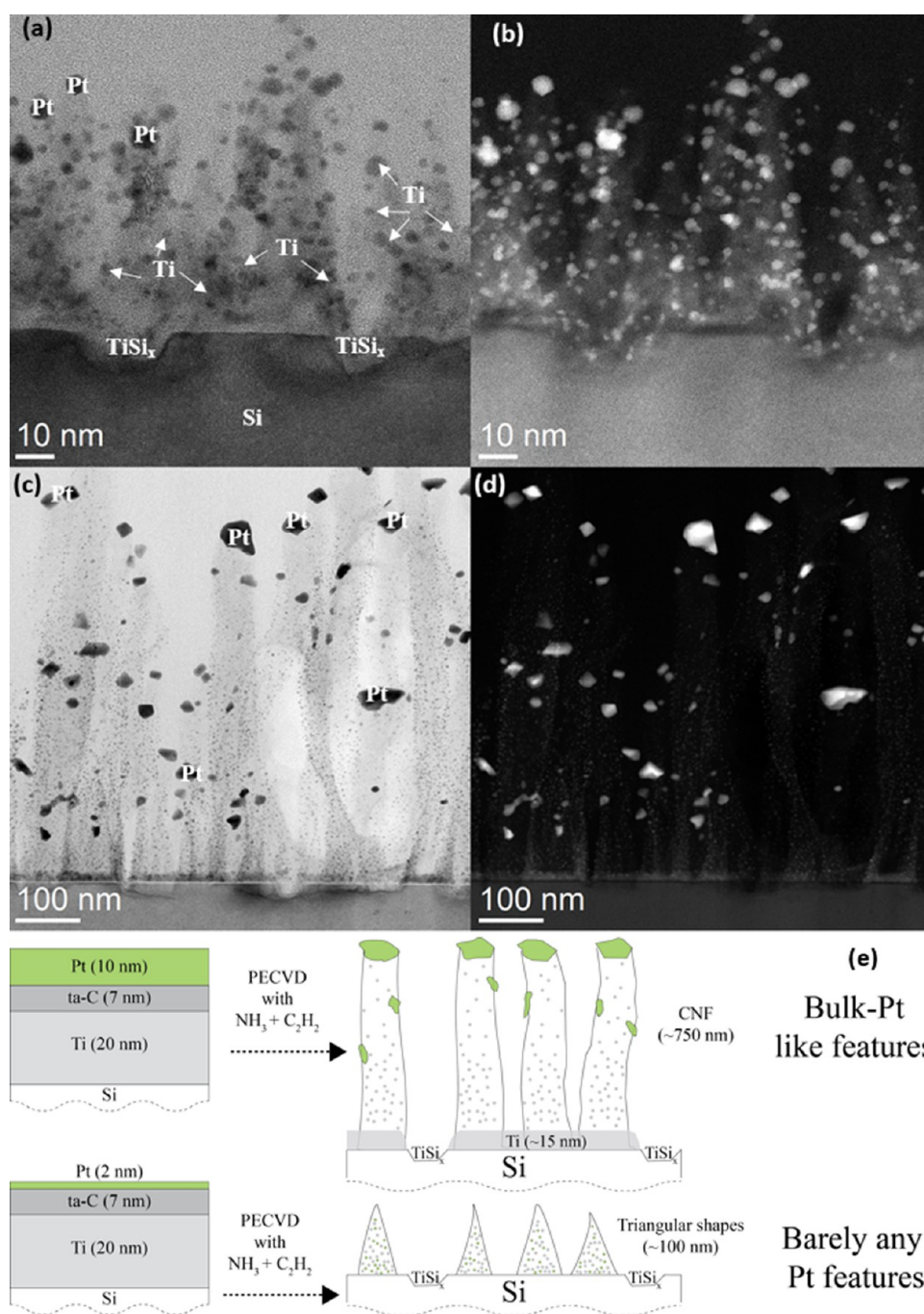


Figure 8. (a, c) Bright-field as well as (b, d) dark-field STEM micrographs showing the resulting structures from the growth process with (a, b) Si/Ti/ta-C/Pt (2 nm) and (c, d) Si/Ti/ta-C/Pt (10 nm) samples. (e) Schematic presentation of the resulting structures.

extremely interesting basis for further applications in biomedical technology, fuel cells, battery technology, and related areas.

EXPERIMENTAL WORK

Synthesis. The CNFs were grown on n-type Si(100)/Ti(20 nm)/ta-C(7 nm)/Pt(2/10 nm). The synthesis can be briefly described as follows: n-type Si (100) wafer substrates (Ultrasil) were mounted by hanging in a rotating carousel (0.04 rpm) in a chamber with a base pressure of 10^{-3} Pa. The expected tetrahedral amorphous carbon (ta-C) film thickness was about 7 nm. Prior to deposition, the wafers were etched with a gridless argon ion source and coated with Ti using a

continuous-current arc source equipped with 60° magnetic filtering. The role of Ti is to ensure excellent adhesion of the ta-C layer on the substrate. A 2 or 10 nm thick Pt catalyst layer was deposited on Ti using cathodic arc deposition. The catalyst-coated wafers were placed in a cold-wall plasma-enhanced chemical vapor deposition (PECVD) reactor (Aixtron, Black Magic, Germany) with the chamber pressure pumped down to <1 Pa, and the samples were annealed at 400°C for 3 min before the growth process was started. The chamber was heated to 400°C by a ramp speed of $250^\circ\text{C}/\text{min}$. After the annealing step, the NH_3 buffer was used to fill the chamber (100 sccm) while the chamber pressure was maintained at 0.1 mbar. The temperature was increased to

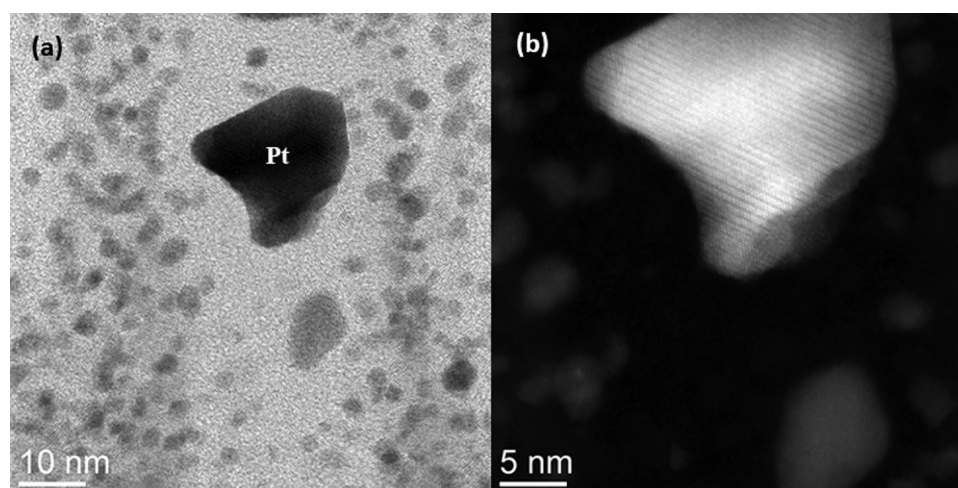


Figure 9. (a) Bright-field and (b) dark-field STEM micrographs showing that Pt particles are in fact single crystals. The small particles seen in the micrographs are mostly Ti.

Table 1. Comparison of the Properties of Amperometric Carbon-Based H₂O₂ Sensors^a

| material | detection potential (V vs Ag/AgCl) | LOD (μM) | sensitivity ($\mu\text{A } \mu\text{M}^{-1} \text{ cm}^{-2}$) | detection time (s) | linear range (μM) | ref |
|--------------------------------|------------------------------------|-----------------------|---|--------------------|--------------------------------|-----------|
| PtNPs/CNT on GC | 0.55 | 0.025 | 3.57 1.85 | N/A | 0.025–10 100–2000 | 36 |
| AgNPs/Chit-GO/cysteamine on Au | −0.442 | 0.7 | N/A | 2 | 6–18 000 | 37 |
| PB/graphene on GC | −0.2 | 0.02 | 1.6 | N/A | 50–5000 | 38 |
| GNPs/SGS on GC | −0.242 | 0.25 | 0.00321 | 3 | 2300–16 000 | 39 |
| Chit-MWCNTs/Hb/AgNPs on GC | −0.3 | 0.347 | N/A | 5 | 6.25–93 | 40 |
| ERGO-ATP-Pd on GC | −0.2 | 0.016 | 0.49209 | 10 | 0.1–10 000 | 41 |
| CNT/PB | 0 | 0.00474 | 31.4 | 5 | 0.05–5 | 42 |
| nanoCoPc-graphene on GC | 0.278 | 10.1 | N/A | 0.2 | 14–63 | 43 |
| Pt/porous graphene on GC | −0.1 | 0.5 | 0.34114 | 3 | 1–1477 | 44 |
| Au@Ag@C nanocomposite on GC | −0.55 | 0.14 8.32 | 0.07602 0.01912 | 5 | 5–75 75–4750 | 45 |
| Au@C@Pt nanocomposite on GC | 0 | 0.13 | 0.1447 0.0801 | 10 | 9–1860 1860–7110 | 46 |
| Pd core-PtNDs/PDDA-rGO on GC | 0.018 | 0.027 | 0.672753 | 5 | 5–500 | 47 |
| CNFs | 0.6 | 66 | 0.0906 | N/A | N/A | 48 |
| MnO ₂ /rGONRs on GC | 0.8 | 0.071 | N/A | several seconds | 0.25–2245 | 49 |
| Mesoporous Pt | 0.45 | 4.5 | 2.8 | N/A | 20–40 000 | 50 |
| Pt nanowires | 0.04 | 0.05 | 0.54 | N/A | 0.1–6000 | 51 |
| Pt-CNFs | −0.1 | 0.000195 | 0.1478 | <0.05 | 10–1000 | this work |

^aPtNP: Pt nanoparticle; AgNP: Ag nanoparticle; Chit: chitosan; GO: graphene oxide; PB: Prussian Blue; GNP: gold nanoparticle; SGS: sulfonated graphene; MWCNT: multiwalled carbon nanotubes; Hb: hemoglobin; ERGO: electrochemically reduced graphene oxide; ATP: aminothiophenol; CoPo: cobalt phthalocyanine; PtND: Pt nanodendrite; PDDA: poly (diallyldimethylammonium chloride); rGO: reduced graphene oxide; rGONR: reduced graphene oxide nanoribbons.

750 °C with a ramp speed of 300 °C/min. After the temperature had reached 675 °C, 150 W DC plasma was ignited while injecting the carbon precursor, C₂H₂, to the chamber (30 sccm) and increasing the NH₃ flow to 125 sccm. The growth phase lasted 10 min and produced vertically aligned fibers that were ~0.2–1 μm tall, as shown in Figure 1a,b, depending on the Pt layer thickness. After the growth process, the pressure was maintained below 0.2 mbar until the temperature decreased to 300 °C.

STEM Analysis. Cross-sectional STEM samples were prepared by focused ion beam (FIB) using first 30 kV for thinning and subsequently 5 kV for final polishing. Polymer ink

was used as the filler material with 70–80 nm of sputtered Pt and FIB-deposited Pt-C to protect the vertical CNF during thinning. HRTEM of the samples was performed using a double-aberration-corrected microscope, JEOL 2100 (JEOL, Japan), equipped with a X-ray EDS operating at 200 kV. A Gatan 4k × 4k UltraScan 4000 CCD camera was employed for digital recording of the HRTEM images.

GIXRD and XRR Measurements. GIXRD and XRR measurements were performed using Rigaku SmartLab diffractometer equipped with a 9 kW rotating Cu anode (1.54 nm wavelength) and HyPix-3000 2D single photon counting detector operated in a 1D mode. All measurements

were conducted in parallel beam mode on $10 \times 10 \text{ mm}^2$ samples with an incidence $K_{\alpha 1}$ monochromator, a 5 mm horizontal slit, and 5° angular aperture Soller slits at both ends. Incidence vertical slit varied according to investigated GIXRD omega angles determined from XRR profiles. Thus, the grazing incidence angles varied from 0.25 to 0.40° with vertical slits of 0.043 – 0.069 mm for the 2 nm Pt sample and from 0.6 to 2.0° with vertical slits of 0.104 – 0.348 for the thicker 10 nm Pt sample. GIXRD scans were performed in steps of 0.2° and $1^\circ/\text{min}$ in the range of 25 – 93° .

Electrochemical Measurements. Cyclic voltammetry and amperometry were performed with a Gamry Reference 600 potentiostat and Gamry Framework software (Gamry Instruments). The reference electrode was a Ag/AgCl/KCl saturated electrode ($+0.199$ vs SHE, Radiometer Analytical) and the counter electrode was a Pt wire in all electrochemical experiments. The samples were dipped in deionized water before the experiments. The electrochemical characteristics were studied in Ar-purged and -blanketed $0.15 \text{ M H}_2\text{SO}_4$. For H_2O_2 experiments, a 100 mM stock solution was freshly prepared from $30\% \text{ H}_2\text{O}_2$ (Merck KGaA, Germany) by diluting in deionized water. The electrochemical cell was filled with PBS (pH 7.4) containing NaCl (137 mM), KCl (2.7 mM), Na_2HPO_4 (10 mM), and KH_2PO_4 (1.8 mM); and the stock solution was added directly to measure different concentrations of H_2O_2 . The sample was cycled in blank PBS between -0.4 and 0.2 V versus Ag/AgCl at 50 mV/s for 10 cycles before the amperometric measurement. The potential was then stepped to -0.1 V versus Ag/AgCl for 180 s. Current densities were calculated using the geometric area of the sample. It should be noted that the actual reactive area might be higher for the Pt-containing CNF.

■ ASSOCIATED CONTENT

🔗 Supporting Information

The Supporting Information is available free of charge on the ACS Publications website at DOI: [10.1021/acsomega.6b00441](https://doi.org/10.1021/acsomega.6b00441).

Elemental maps (EDS-maps) from the two types of Pt samples (Figures S1 and S2), XRR spectra from the two types of Pt samples (Figure S3), as well as a Raman spectra showing the effect of hydrogen and acetylene on the ta-C layer of different thicknesses (Figure S4) (PDF)

■ AUTHOR INFORMATION

Corresponding Author

*E-mail: tomi.laurila@aalto.fi. Tel: +358 50 3414375.

ORCID

Tomi Laurila: [0000-0002-1252-8764](https://orcid.org/0000-0002-1252-8764)

Notes

The authors declare no competing financial interest.

■ ACKNOWLEDGMENTS

The authors T.L. and S.S. acknowledge funding from Academy of Finland (grant numbers 285015 and 285526). Professor Krisztian Kordas and Olli Pitkänen from University of Oulu are acknowledged for Raman analyses. We acknowledge the provision of facilities and technical support by Aalto University at OtaNano - Nanomicroscopy Center (Aalto-NMC).

■ REFERENCES

- (1) Gamez, A.; Richard, D.; Gallezot, P.; Gloaguen, F.; Faure, R.; Durand, R. Oxygen reduction on well-defined platinum nanoparticles inside recast ionomer. *Electrochim. Acta* **1996**, *41*, 307–314.
- (2) Wroblowa, H. S.; Razumney, G. Electroreduction of oxygen: A new mechanistic criterion. *J. Electroanal. Chem. Interfacial Electrochem.* **1976**, *69*, 195–201.
- (3) Schneider, A.; Colmenares, L.; Seidel, Y. E.; Jusys, Z.; Wickman, B.; Kasemo, B.; Behm, R. J. Transport effects in the oxygen reduction reaction on nanostructured, planar glassy carbon supported Pt/GC model electrodes. *Phys. Chem. Chem. Phys.* **2008**, *10*, 1931–1943.
- (4) Gibson, Q. H.; Swoboda, B. E. P.; Massey, V. Kinetics and Mechanism of Action of Glucose Oxidase of Action of Glucose. *J. Biol. Chem.* **1964**, *239*, 3927–3934.
- (5) Kusakabe, H.; Midorikawa, Y.; Fujishima, T.; Kuninaka, A.; Yoshino, H. Purification and properties of a new enzyme, l-glutamate oxidase, from *Streptomyces* sp. X-119-6 grown on wheat bran. *Agric. Biol. Chem.* **1983**, *47*, 1323–1328.
- (6) Yue, Q. K.; Kass, I. J.; Sampson, N. S.; Vrieling, A. Crystal structure determination of cholesterol oxidase from *Streptomyces* and structural characterization of key active site mutants. *Biochemistry* **1999**, *38*, 4277–4286.
- (7) Katsounaros, I.; Schneider, W. B.; Meier, J. C.; Benedikt, U.; Biedermann, P. U.; Auer, A. A.; Mayrhofer, K. J. Hydrogen peroxide electrochemistry on platinum: towards understanding the oxygen reduction reaction mechanism. *Phys. Chem. Chem. Phys.* **2012**, *14*, 7384–7391.
- (8) Sitta, E.; Feliu, J. M. The role of PtOH on H_2O_2 interactions with platinum surfaces in an electrochemical environment. *ChemElectroChem* **2014**, *1*, 55–58.
- (9) Gómez-Marín, A. M.; Rizo, R.; Feliu, J. M. Some reflections on the understanding of the oxygen reduction reaction at Pt (111). *Beilstein J. Nanotechnol.* **2013**, *4*, 956–967.
- (10) Sitta, E.; Gómez-Marín, A. M.; Aldaz, A.; Feliu, J. M. Electrocatalysis of H_2O_2 reduction/oxidation at model platinum surfaces. *Electrochem. Commun.* **2013**, *33*, 39–42.
- (11) Besteman, K.; Lee, J. O.; Wiertz, F. G.; Heering, H. A.; Dekker, C. Enzyme-coated carbon nanotubes as single-molecule biosensors. *Nano Lett.* **2003**, *3*, 727–730.
- (12) Karajanagi, S. S.; Vertegel, A. A.; Kane, R. S.; Dordick, J. S. Structure and function of enzymes adsorbed onto single-walled carbon nanotubes. *Langmuir* **2004**, *20*, 11594–11599.
- (13) Wang, J. Carbon-nanotube based electrochemical biosensors: A review. *Electroanalysis* **2005**, *17*, 7–14.
- (14) Baker, S. E.; Colavita, P. E.; Tse, K. Y.; Hamers, R. J. Functionalized vertically aligned carbon nanofibers as scaffolds for immobilization and electrochemical detection of redox-active proteins. *Chem. Mater.* **2006**, *18*, 4415–4422.
- (15) Vamvakaki, V.; Tsagaraki, K.; Chaniotakis, N. Carbon nanofiber-based glucose biosensor. *Anal. Chem.* **2006**, *78*, 5538–5542.
- (16) Wang, J.; Liu, G.; Jan, M. R. Ultrasensitive electrical biosensing of proteins and DNA: carbon-nanotube derived amplification of the recognition and transduction events. *J. Am. Chem. Soc.* **2004**, *126*, 3010–3011.
- (17) Meyyappan, M. Nano biosensors for neurochemical monitoring. *Nano Convergence* **2015**, *2*, 18.
- (18) Chakraborty, S.; Raj, C. R. Amperometric biosensing of glutamate using carbon nanotube based electrode. *Electrochem. Commun.* **2007**, *9*, 1323–1330.
- (19) Isoaho, N.; Peltola, E.; Sainio, S.; Wester, N.; Protopopova, V.; Koskinen, J.; Laurila, T. Carbon nanostructure based platform for enzymatic biosensors. *J. Phys. Chem. C*, in press, **2017**.
- (20) Sainio, S.; Jiang, H.; Caro, M. A.; Koehne, J.; Lopez-Acevedo, O.; Koskinen, J.; Laurila, T. Structural morphology of carbon nanofibers grown on different substrates. *Carbon* **2016**, *98*, 343–351.
- (21) Laurila, T.; Sainio, S.; Jiang, H.; Koskinen, J.; Koehne, J.; Meyyappan, M. The role of extra carbon source during the pre-annealing stage in the growth of carbon nanofibers. *Carbon* **2016**, *100*, 351–354.

- (22) Conway, B. E.; Angerstein-Kozłowska, H.; Sharp, W. B. A.; Criddle, E. E. Ultrapurification of water for electrochemical and surface chemical work by catalytic pyrodistillation. *Anal. Chem.* **1973**, *45*, 1331–1336.
- (23) Wieboldt, R.; Gee, K. R.; Niu, L.; Ramesh, D.; Carpenter, B. K.; Hess, G. P. Photolabile precursors of glutamate: synthesis, photochemical properties, and activation of glutamate receptors on a microsecond time scale. *Proc. Natl. Acad. Sci. U.S.A.* **1994**, *91*, 8752–8756.
- (24) Laurila, T.; Protopopova, V.; Rhode, S.; Sainio, S.; Palomäki, T.; Moram, M.; Koskinen, J. New electrochemically improved tetrahedral amorphous carbon films for biological applications. *Diamond Relat. Mater.* **2014**, *49*, 62–71.
- (25) Laurila, T.; Sainio, S.; Jiang, H.; Palomäki, T.; Pitkänen, O.; Kordas, K.; Koskinen, J. Multi-walled carbon nanotubes (MWCNTs) grown directly on tetrahedral amorphous carbon (ta-C): An interfacial study. *Diamond Relat. Mater.* **2015**, *56*, 54–59.
- (26) Swanson, H. E.; Tatge, E.; Fuyat, R. K. Standard X-ray diffraction powder patterns, 1953.
- (27) Ming, L. C.; Manghnani, M. H.; Katahara, K. W. Phase transformations in the Ti-V system under high pressure up to 25 GPa. *Acta Metall.* **1981**, *29*, 479–485.
- (28) Hubbard, C. R.; Swanson, H. T.; Mauer, F. A. A silicon powder diffraction standard reference material. *J. Appl. Crystallogr.* **1975**, *8*, 45–48.
- (29) Han, J. H.; Choi, S. H.; Lee, T. Y.; Yoo, J. B.; Park, C. Y.; Jung, T.; Kim, J. M. Growth characteristics of carbon nanotubes using platinum catalyst by plasma enhanced chemical vapor deposition. *Diamond Relat. Mater.* **2003**, *12*, 878–883.
- (30) Yazzev, O. V.; Pasquarello, A. Effect of metal elements in catalytic growth of carbon nanotubes. *Phys. Rev. Lett.* **2008**, *100*, No. 156102.
- (31) Towell, G. D.; Martin, J. J. Kinetic data from nonisothermal experiments: Thermal decomposition of ethane, ethylene, and acetylene. *AIChE J.* **1961**, *7*, 693–698.
- (32) Tae Hwang, J.; Shik Chung, J. The morphological and surface properties and their relationship with oxygen reduction activity for platinum-iron electrocatalysts. *Electrochim. Acta* **1993**, *38*, 2715–2723.
- (33) Han, B. C.; Miranda, C. R.; Ceder, G. Effect of particle size and surface structure on adsorption of O and OH on platinum nanoparticles: A first-principles study. *Phys. Rev. B: Condens. Matter Mater. Phys.* **2008**, *77*, 1–9.
- (34) Mayrhofer, K. J. J.; Blizanac, B. B.; Arenz, M.; Stamenkovic, V. R.; Ross, P. N.; Markovic, N. M. The impact of geometric and surface electronic properties of Pt-catalysts on the particle size effect in electrocatalysis. *J. Phys. Chem. B* **2005**, *109*, 14433–14440.
- (35) Climent, V.; Feliu, J. M. Thirty years of platinum single crystal electrochemistry. *J. Solid State Electrochem.* **2011**, *15*, 1297–1315.
- (36) Hrapovic, S.; Liu, Y.; Male, K. B.; Luong, J. H. T. Electrochemical Biosensing Platforms Using Platinum Nanoparticles and Carbon Nanotubes. *Anal. Chem.* **2004**, *76*, 1083–1088.
- (37) Wang, L.; Zhu, H.; Hou, H.; Zhang, Z.; Xiao, X.; Song, Y. A Novel Hydrogen Peroxide Sensor Based on Ag Nanoparticles Electrodeposited on Chitosan-Graphene Oxide/cysteamine-Modified Gold Electrode. *J. Solid State Electrochem.* **2012**, *16*, 1693–1700.
- (38) Li, S. J.; Du, J. M.; Shi, Y. F.; Li, W. J.; Liu, S. R. Functionalization of Graphene with Prussian Blue and Its Application for Amperometric Sensing of H₂O₂. *J. Solid State Electrochem.* **2012**, *16*, 2235–2241.
- (39) Li, S. J.; Shi, Y. F.; Liu, L.; Song, L. X.; Pang, H.; Du, J. M. Electrostatic Self-Assembly for Preparation of Sulfonated Graphene/gold Nanoparticle Hybrids and Their Application for Hydrogen Peroxide Sensing. *Electrochim. Acta* **2012**, *85*, 628–635.
- (40) Li, Y.; Li, Y.; Yang, Y. A New Amperometric H₂O₂ Biosensor Based on Nanocomposite Films of chitosan–MWNTs, Hemoglobin, and Silver Nanoparticles. *J. Solid State Electrochem.* **2011**, *16*, 1133–1140.
- (41) You, J. M.; Kim, D.; Kim, S. K.; Kim, M. S.; Han, H. S.; Jeon, S. Novel Determination of Hydrogen Peroxide by Electrochemically Reduced Graphene Oxide Grafted with Aminothiophenol-Pd Nanoparticles. *Sens. Actuators, B* **2013**, *178*, 450–457.
- (42) Husmann, S.; Nossol, E.; Zarbin, A. J. G. Carbon nanotube/Prussian Blue Paste Electrodes: Characterization and Study of Key Parameters for Application as Sensors for Determination of Low Concentration of Hydrogen Peroxide. *Sens. Actuators, B* **2014**, *192*, 782–790.
- (43) Wang, H.; Bu, Y.; Dai, W.; Li, K.; Wang, H.; Zuo, X. Well-Dispersed Cobalt Phthalocyanine Nanorods on Graphene for the Electrochemical Detection of Hydrogen Peroxide and Glucose Sensing. *Sens. Actuators, B* **2015**, *216*, 298–306.
- (44) Liu, J.; Bo, X.; Zhao, Z.; Guo, L. Highly Exposed Pt Nanoparticles Supported on Porous Graphene for Electrochemical Detection of Hydrogen Peroxide in Living Cells. *Biosens. Bioelectron.* **2015**, *74*, 71–77.
- (45) Li, Y.; Zhang, Y.; Zhong, Y.; Li, S. Enzyme-Free Hydrogen Peroxide Sensor Based on Au@Ag@C Core-Double Shell Nanocomposites. *Appl. Surf. Sci.* **2015**, *347*, 428–434.
- (46) Zhang, Y.; Li, Y.; Jiang, Y.; Li, Y.; Li, S. The Synthesis of Au@C@Pt Core-Double Shell Nanocomposite and Its Application in Enzyme-Free Hydrogen Peroxide Sensing. *Appl. Surf. Sci.* **2016**, *378*, 375–383.
- (47) Zhang, Y.; Zhang, C.; Zhang, D.; Ma, M.; Wang, W.; Chen, Q. Nano-Assemblies Consisting of Pd/Pt Nanodendrites and Poly (Diallyldimethylammonium Chloride)-Coated Reduced Graphene Oxide on Glassy Carbon Electrode for Hydrogen Peroxide Sensors. *Mater. Sci. Eng., C* **2016**, *58*, 1246–1254.
- (48) Suazo-Dávila, D.; Rivera-Meléndez, J.; Koehne, J.; Meyyappan, M.; Cabrera, C. R. Surface Analysis and Electrochemistry of a Robust Carbon-Nanofiber-Based Electrode Platform H₂O₂ Sensor. *Appl. Surf. Sci.* **2016**, *384*, 251–257.
- (49) Wu, Z.-L.; Li, C.-K.; Yu, J.-G.; Chen, X.-Q. MnO₂/reduced Graphene Oxide Nanoribbons: Facile Hydrothermal Preparation and Their Application in Amperometric Detection of Hydrogen Peroxide. *Sens. Actuators, B* **2017**, *239*, 544–552.
- (50) Evans, S. A.; Elliott, J. M.; Andrews, L. M.; Bartlett, P. N.; Doyle, P. J.; Denuault, G. Detection of hydrogen peroxide at mesoporous platinum microelectrodes. *Anal. Chem.* **2002**, *74*, 1322–1326.
- (51) Yang, M.; Qu, F.; Lu, Y.; He, Y.; Shen, G.; Yu, R. Platinum nanowire nanoelectrode array for the fabrication of biosensors. *Biomaterials* **2006**, *27*, 5944–5950.
- (52) Palomäki, T.; Chumillas, S.; Sainio, S.; Protopopova, V.; Kauppila, M.; Koskinen, J.; Laurila, T. Electrochemical reactions of catechol, methylcatechol and dopamine at tetrahedral amorphous carbon (ta-C) thin film electrodes. *Diamond Relat. Mater.* **2015**, *59*, 30–39.
- (53) Chumillas, S.; Figueiredo, M. C.; Climent, V.; Feliu, J. M. Study of dopamine reactivity on platinum single crystal electrode surfaces. *Electrochim. Acta* **2013**, *109*, 577–586.
- (54) Sainio, S.; Palomäki, T.; Tujunen, N.; Protopopova, V.; Koehne, J.; Kordas, K.; Laurila, T. Integrated carbon nanostructures for detection of neurotransmitters. *Mol. Neurobiol.* **2015**, *52*, 859–866.
- (55) Huang, J.; Hou, H.; You, T. Highly efficient electrocatalytic oxidation of formic acid by electrospun carbon nanofiber-supported Pt_xAu_{100-x} bimetallic electrocatalyst. *Electrochem. Commun.* **2009**, *11*, 1281–1284.
- (56) Xuyen, N. T.; Jeong, H. K.; Kim, G.; So, K. P.; An, K. H.; Lee, Y. H. Hydrolysis-induced immobilization of Pt (acac)₂ on polyimide-based carbon nanofiber mat and formation of Pt nanoparticles. *J. Mater. Chem.* **2009**, *19*, 1283–1288.
- (57) Yang, T.; Du, M.; Zhu, H.; Zhang, M.; Zou, M. Immobilization of Pt nanoparticles in carbon nanofibers: bifunctional catalyst for hydrogen evolution and electrochemical sensor. *Electrochim. Acta* **2015**, *167*, 48–54.